

Article

# Thermal Stability of Rare Earth-PYSZ Thermal Barrier Coating with High-Resolution Transmission Electron Microscopy

Savisha Mahalingam <sup>1,\*</sup>, Abreeza Manap <sup>2</sup>, Salmi Mohd Yunus <sup>3</sup> and Nurfanizan Afandi <sup>2</sup>

<sup>1</sup> Institute of Sustainable Energy, Universiti Tenaga Nasional, Jalan IKRAM-UNITEN, Kajang 43000, Selangor, Malaysia

<sup>2</sup> College of Engineering, Universiti Tenaga Nasional, Jalan IKRAM-UNITEN,

Kajang 43000, Selangor, Malaysia; abreeza@uniten.edu.my (A.M.); nurfanizan@uniten.edu.my (N.A.)

<sup>3</sup> Materials Engineering & Testing Group, TNB Research Sdn Bhd,

No1 Lorong Ayer Itam Kawasan Institusi Penyelidikan, Kajang 43000, Selangor, Malaysia;

salmi.yunus@tnb.com.my

\* Correspondence: savisha@uniten.edu.my; Tel.: +60-03-89212020

Received: 17 November 2020; Accepted: 7 December 2020; Published: 10 December 2020



**Featured Application:** Thermal barrier coating is applied to aviation turbines to protect the nickel-based superalloys from melting and thermal cycling.

**Abstract:** Durability of a thermal barrier coating (TBC) depends strongly on the type of mixed oxide in the thermally grown oxide (TGO) of a TBC. This study aims on discovering the effect of thermal stability in the TGO area containing mixed oxides. Two different bondcoats were studied using high-resolution transmission electron microscopy: high-velocity oxygen fuel (HVOF) and air-plasma spray (APS), under isothermal and thermal cyclic tests at 1400 °C. The HVOF bondcoats were intact until 1079 cycles. In comparison, APS failed at the early stage of thermal cycling at 10 cycles. The phase transformation of topcoat from tetragonal to the undesired monoclinic was observed, leading to TBC failure. The results showed that the presence of transient aluminas found in HVOF bondcoat helps in the slow growth of  $\alpha$ -Al<sub>2</sub>O<sub>3</sub>. In contrast, the APS bondcoat does not contain transient aluminas and transforms quickly to  $\alpha$ -Al<sub>2</sub>O<sub>3</sub> along with spinel and other oxides. This fast growth of mixed oxides causes stress at the interface (topcoat and TGO) and severely affects the TBC durability leading to early failure. Therefore, the mixed oxide with transient aluminas slows down the quick transformation into alpha-aluminas, which provides high thermal stability for a high TBC durability.

**Keywords:** high-velocity oxygen fuel; high-resolution transmission electron microscopy; mixed oxides; transient aluminas

## 1. Introduction

Thermal barrier coatings (TBCs) have been applied to the high-temperature section of engines to improve the performance of the gas turbine engine. Typical TBCs contain a three-layered material system, consisting of (1) 6–8 wt.% of partially yttria-stabilized zirconia (PYSZ) topcoat deposited most commonly via an air-plasma spray (APS) process; (2) bondcoat to resist the oxidation of Ni-based superalloy substrates; and (3) a superalloy substrate (nickel or cobalt). Industrial turbines commonly operate at a turbine inlet temperature 1300 °C, and the aero-engines operate at 1400 °C [1]. Currently, Japan is working towards 1700 °C class high-efficiency gas turbines to enhance the combined cycle plant [2]. Although TBCs exposed to temperatures above 1200 °C are less resistant to oxidation and decrease their mechanical properties [3], they often face premature failure, undergoing a phase

transformation supported by a 4–6% volume expansion combustion atmosphere [4]. The failure is due to the thermally grown oxide (TGO) layer which is formed between the metallic bondcoat and topcoat due to the oxidation of bondcoat at high temperatures.

The TGO layer can be protective and also harmful at the same time, depending on its thickness. A uniform and dense protective layer of stable  $\text{Al}_2\text{O}_3$  can be beneficial to the system [5]. However, the high-temperature exposure causes high oxidation in the bondcoat leading to a thicker TGO layer causing volume expansion towards the topcoat above it and fails. Surprisingly, in TBC systems where the bondcoat has wholly transformed into oxide (thick TGO) under service, the topcoat is still intact. Thus, the ultimate reason for the failure is the mixed oxide content present in the TGO [6], and it gets even worse under cyclic thermal exposure.

Generally, after cooling during cyclic thermal exposure, TBCs frequently fail due to the compressive residual stress between the bondcoat and TGO accompanied by stress arising from TGO growth, causing spallation [7]. Spallation is the peeling of TBC, and it mainly happens due to the stresses with the growth of TGO and misfit stress at the bondcoat/topcoat interface. There are also other reasons for TBC spallation, such as calcium-magnesium-aluminum-silicon oxide systems, commonly known as CMAS [8], which will not be discussed in this article. This stress is due to the mixed oxides containing  $\text{Al}_2\text{O}_3$ ,  $\text{Cr}_2\text{O}_3$ ,  $\text{Ni}(\text{Cr}, \text{Al})\text{O}_2$ ,  $\text{Ni}(\text{Cr}, \text{Al})$ , and  $\text{NiO}$ .  $\text{Ni}(\text{Cr}, \text{Al})\text{O}_2$  and  $\text{Ni}(\text{Cr}, \text{Al})$  are called as spinel. These mixed oxides with spinel and  $\text{NiO}$  forms segmented TGO ( $\text{Al}_2\text{O}_3$ ) layer causes high tensile stress, leading to the separation of the ceramic layer from the bondcoat [9,10]. This is because oxygen diffusion through spinel and  $\text{NiO}$  is faster through  $\text{Al}_2\text{O}_3$  [10]. A continuous TGO layer with low oxygen diffusivity and slow growth of  $\text{Al}_2\text{O}_3$  can inhibit the permeation of Ni, Cr, Al, and O (delaying further bondcoat oxidation) [10]. However, the phase-type of aluminas formed in the TGO also influences the TBC durability.

A stable  $\alpha\text{-Al}_2\text{O}_3$  protects the bondcoat and ensures a stronger bond between the bondcoat and topcoat, promoting a slow growth rate due to the low diffusion rate of Oxygen through the TGO [11]. Non-alpha-alumina ( $\gamma$ ,  $\theta$ , and  $\eta$ ) or also known as transient aluminas formation may lead to volumetric expansion or contraction and premature tensile cracking in the TGO, failing the TBC [12]. The transient aluminas continues to grow outward and transforms to the equilibrium  $\alpha\text{-Al}_2\text{O}_3$ , and the zone formation ceases when the transformation to  $\alpha\text{-Al}_2\text{O}_3$  occurs [13]. The TGO consists of inner (TGO/belowTGO) and outer layers (topcoat/TGO). Usually, the transient aluminas form at the inner layer, and the alpha-alumina with particles of Zr and Y are present at the outer layer. Kobayashi et al. reported that the quick phase transformation from  $\gamma\text{-Al}_2\text{O}_3$  to  $\alpha\text{-Al}_2\text{O}_3$  might increase residual stress and eventually reduces the lifetime of TBC [14]. There are several ways for microstructural evaluation and thermal stability for TBCs.

In this regard, microstructural evaluation through scanning electron microscopy (SEM), X-ray diffraction, and energy dispersive spectroscopy (EDS) have traditionally been undertaken to examine the TBC failure by TGO spallation [15–18]. Although these methods offer benefits in understanding TBC failure, limitations in resolving the instruments, and specimen destruction during sample preparation impede these applications. During the past few decades, high-resolution transmission electron microscopy (HRTEM) has been used to study thermal stability directly or through in-situ experiments for TBCs [19].

However, HRTEM has been rarely used for thermal stability evaluation of TBCs, mainly due to the inconvenience in specimen preparation, since the region of interest needs to be intact and sufficiently thin to be observed through HRTEM [20,21]. Accordingly, the focused ion beam (FIB) technique has been employed for specimen preparation of HRTEM predominantly for specimens containing fragile interfaces such as TBC coated systems. Nevertheless, numerous research studies have been carried out on alternate ceramics aside from PYSZ with increased thermal stability in addition to initiating lower thermal conductivity [22–24]. For instance, co-doped zirconates with rare earth material such as lanthanum (La) exhibited high durability due to high fusion enthalpy [25]. La and gadolinium (Gd)

combination in TBC possesses low thermal conductivity, low sintering rate, and high thermal stability up to 2300 °C [26].

Although numerous pieces of research have focused on rare earth-PYSZ topcoats, the compatible bondcoat remains a significant challenge, since the bondcoat also plays an essential role by providing extra adhesion of the topcoat to the substrate. Moreover, many processes have been employed to deposit bondcoat, such as APS, low-pressure plasma spray, and high-velocity oxygen fuel (HVOF) [27]. The APS technique is the most popular to form bondcoat due to its economic benefits; however, the HVOF process is more desirable to increase the working temperature and fuel performance in gas turbines and diesel engines [28,29]. According to Lu et al., more extended thermal durability was found in HVOF bondcoat than in the APS bondcoat due to lower equivalent stress at the TGO layer [28]. However, most HVOF bondcoating does not focus on the phase transformation of alumina in TGO and the stress-induced at the interface of topcoat and bondcoat simultaneously.

Therefore, this study investigates the thermal stability using lattice fringes (phase stability). Although this method has been employed in the literature to a certain extent, the study on the full area of TGO has not been investigated. As such, this study presents an evaluation of thermal stability on PYSZ topcoat at the entire area of TGO, starting from the TGO near the topcoat until reaching the bottom near the bondcoat. This study investigates the influence of bondcoat species at a temperature of 1400 °C for both isothermal and cyclic thermal exposure on the TBC's lifetime of the rare earth–yttria-stabilized zirconia (RE-PYSZ) TBC system. Two types of bondcoats (APS and HVOF) were prepared for APS TBCs

## 2. Materials and Methods

The specimens were square-shaped, with dimensions of 60 mm × 60 mm × 6mm. Preparation of the samples was undertaken by applying different deposition techniques for the bondcoats, while identical deposition techniques for topcoats were involved in each case. The ceramic topcoat used was Y-5 wt.%, Zr-65 wt.%, La-0.15 wt.%, and Gd-0.1 wt.% deposited via the APS technique. The RE-PYSZ topcoat was prepared via the APS method employing nitrogen as the primary plasma gas, hydrogen as secondary plasma gas, and argon as the carrier gas with a powder feed rate of 55 g/min and a spraying distance of 90 mm. The bondcoat consisted of Ni-Cr-Al-Y elements generated by using APS and HVOF spraying systems, and the coatings were deposited on a Ni-base superalloy, Nimonic 263 (Nim263). The preparation parameters for APS and HVOF techniques were tabulated in Table 1. Besides, the repeatability of each analysis for both test conditions under isothermal and thermal cycling is three times per sample.

**Table 1.** Preparation parameters for APS and HVOF techniques.

| Parameter                      | Unit           | APS | HVOF |
|--------------------------------|----------------|-----|------|
| Arc Current                    | Amps           | 575 | -    |
| Primary plasma gas, Nitrogen   | NLPM           | 35  | -    |
| Primary plasma gas, Oxygen     | NLPM           | -   | 800  |
| Secondary plasma gas, Hydrogen | NLPM           | 10  | -    |
| Carrier gas, Argon             | NLPM           | 3.0 | 9.0  |
| Powder feed rate               | g/min          | 55  | -    |
| Spraying distance              | mm             | 90  | -    |
| Stirrer                        | % of max speed | 80  | -    |
| Fuel (Kerosene)                | Litre/hour     | -   | 18   |
| Disc rotation                  | % of max speed | -   | 8.0  |

Both the APS and HVOF applied in this work were obtained from Flame Spray Technologies B.V., Duiven, the Netherlands, and using an MP-100 with robot manipulation of 6-axes ABB IRB2400/16. However, they use a different type of gun, whereas APS uses an F4-MB Plasma Gun with a 6 mm nozzle diameter, and HVOF uses a JP5000 Liquid Fuel Gun. The sample abbreviation of the TBC samples used in this work is listed in Table 2.

**Table 2.** TBC sample abbreviations.

| Temperature (°C)           | Hours /Cycles              | APS   | HVOF   |
|----------------------------|----------------------------|-------|--------|
| As-applied                 | -                          | A     | H      |
| 1400 (Isothermal test)     | 100 h                      | A100h | H100h  |
| 1400 (Thermal cyclic test) | 5 Cycles                   | A5c   | H5c    |
|                            | 10 Cycles                  | A10c  | H10c   |
|                            | 1080 Cycles (Until failed) | -     | H1080c |

### 2.1. Isothermal Test

The samples were put into a furnace, which is kept at 150 °C and then a hot gas of 1400° C is flown over the sample continuously for 100 h. The specimens were then furnace cooled and removed once cooling was complete to prevent thermal shock.

### 2.2. Thermal Cycle Test

The tip of the flame was positioned in the middle of the specimen surface with the topcoat facing upwards. The rise of the specimen surface temperature was monitored through the temperature indicator shown in the control panel. When the temperature reached 1400 °C, the specimen was allowed to heat for five minutes. Upon that time, the cutting torch was shut off by closing the acetylene blowpipe valve, followed by closing the oxygen blowpipe valve. The pressurized air valve was then immediately opened to allow the specimens to cool down until reaching 100 °C. This entire process was counted as one cycle. The whole process was repeated for 5 cycles until the specimen failed. In other words, the thermal cycle test concluded when the condition of the specimen presented signs of failure. Figure 1 shows the process of TBC failure applying the thermal cycle test for (a) APS-bondcoat and (b) HVOF-bondcoat samples.

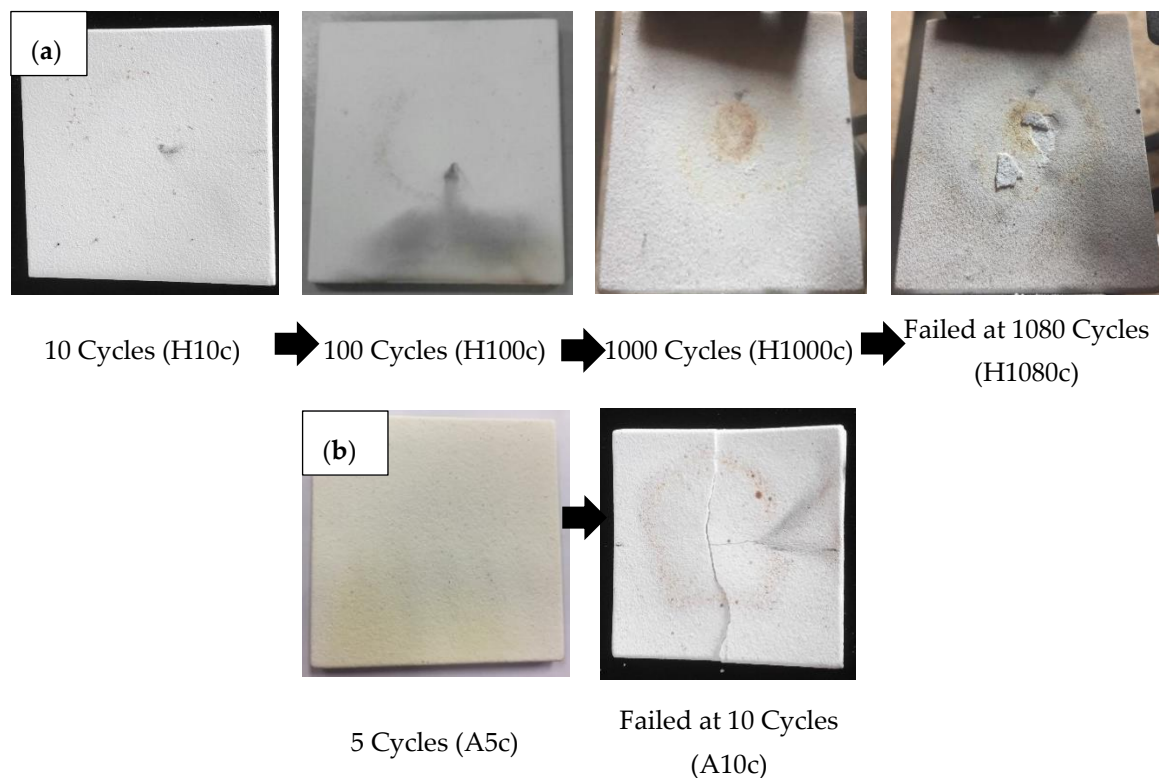


**Figure 1.** Process of TBC failure by thermal cycle test for (a) HVOF and (b) APS bondcoats.

### 2.3. Characterization

The microstructural analysis was carried out using SEM equipped with EDS (JEOL JSM 6010 LA/LV, Universiti Tenaga Nasional, Kajang, Malaysia) and HRTEM (JEOL JEM-2100F, 200 kV, Universiti Putra Malaysia, Serdang, Malaysia) instruments. The thermal stability (phase analysis) and strain caused by thermal exposure were analyzed via HRTEM.

### 2.4. Sample Preparation for SEM and HRTEM

The specimens for SEM and HRTEM were prepared employing two steps: (1) cutting; and (2) grinding and polishing. Sample preparation for HRTEM was further conducted using in-situ FIB micromachining. The specimens were cross-sectioned to 20 mm × 5 mm × 5 mm to characterize using a manual milling machine and surface finishing process. Then rough grinding and polishing were conducted as showed in Figure S1. The FIB process included eight stages: (1) EDS mapping (location finding of the TBC interface with the topcoat, TGO, and bondcoat); (2) E-beam platinum deposition (to protect the top portion of the specimen and to mark the position of the target area); (3) I-beam platinum deposition (to protect the top part of the specimen and to mark the location of the target area); (4) bulk milling (high beam currents are used to mill large amounts of material away from the front and back of the region of interest); (5) J-cut (the bottom and right edge are cut free leaving just a small tab of material on the left side holding the lamellae); (6) lift-out (the easy lift needle is attached to the lamellae using Pt deposition, and the sample is lifted out of the bulk material); (7) mounting (lamellae is connected to the copper grid at 0° tilt), and (8) thinning (lamellae is thinned to < 100 nm). FIB process including all eight stages are shown in Figure S2.

### 2.5. Thermal Stability and Strain Measurement with HRTEM

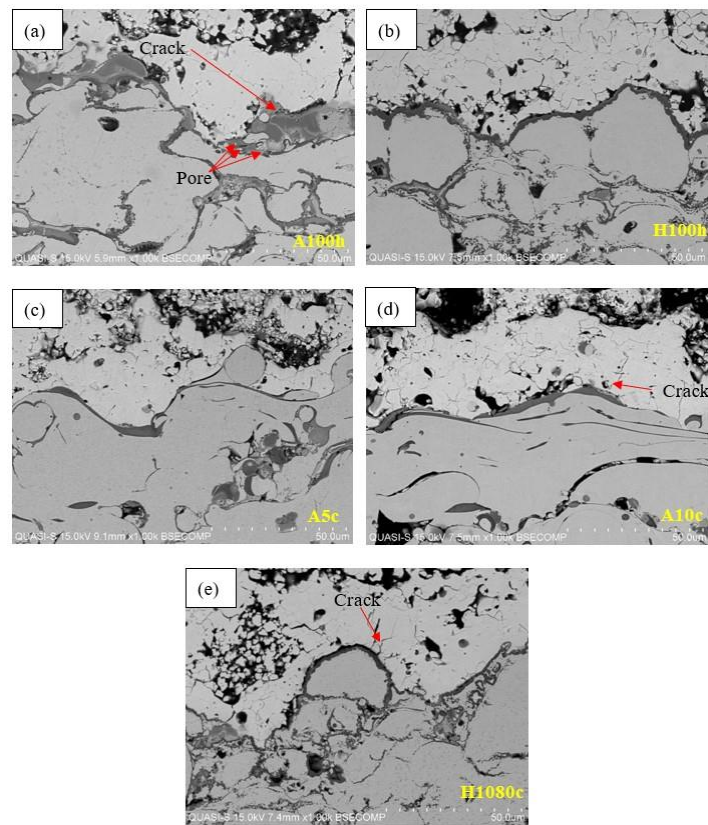
The lamella obtained from FIB micromachining was observed through HRTEM. The thermal stability was examined by analyzing the phases of alumina in each area from the topcoat (near to TGO), TGO, and bondcoat (near to the TGO) through the lattice fringes.

## 3. Results

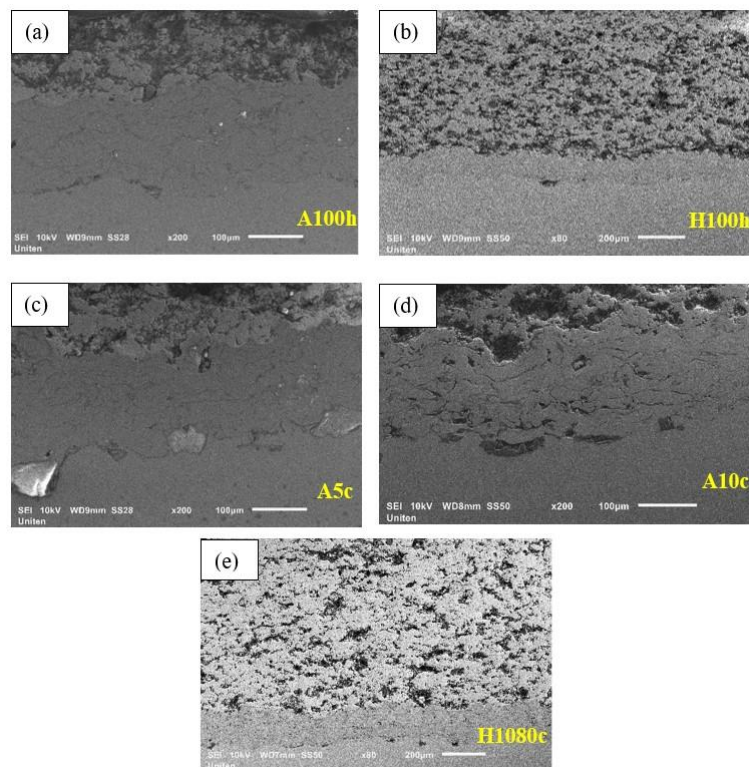
### 3.1. Microstructure and TGO Growth

Figure 2 shows the cracks and pores on the samples. At a high temperature of 1400 °C, the TGO layer of APS-bondcoat could not maintain a continuous TGO layer (Figure 3a,c,d) due to aluminum (Al) depletion and, consequently, forms more mixed oxide growth. On the other hand, the HVOF-bondcoat (Figure 3b,e) developed a continuous TGO, given it suffered less oxidation with thinner TGO growth. The continuous TGO layer, in this case, protected the bondcoat from further oxidation to form harmful mixed oxides and consequently improving its durability. SEM/EDS semi-quantitative analysis showed that the TGO of both bondcoats samples consisted of mixed oxide ( $\text{Ni}(\text{Al}, \text{Cr})_2\text{O}_4$ ) and zirconia (Zr) with a low concentration of chromium (Cr). According to previous studies [30,31], the composition of Ni with 13–16 wt.% and Cr < 10wt.% indicates spinel nickel aluminate ( $\text{NiAl}_2\text{O}_4$ ), which occurs when Al and Cr have been consumed continuously below the detection threshold. At a lower Cr concentration (Cr < 10 wt.%), Ni reacts with  $\text{Al}_2\text{O}_3$  to produce  $\text{NiAl}_2\text{O}_4$ .

The high mixed oxide thickness ratio confirms a high amount of spinel in the TGO layer of APS-bondcoat (Figure 4 and Table 3). Additionally,  $\text{Al}_2\text{O}_3$  thickness ratio refers to the percentage of alumina thickness vs. mixed oxide thickness within an entire TGO thickness.



**Figure 2.** SEM micrographs of isothermal (a) A100h, and (b) H100h and thermal cyclic test (c) A5c, (d) A10c, and (e) H1080c.



**Figure 3.** Wide view image of SEM micrograph, of isothermal (a) A100h, and (b) H100h and thermal cyclic test (c) A5c, (d) A10c, and (e) H1080c.

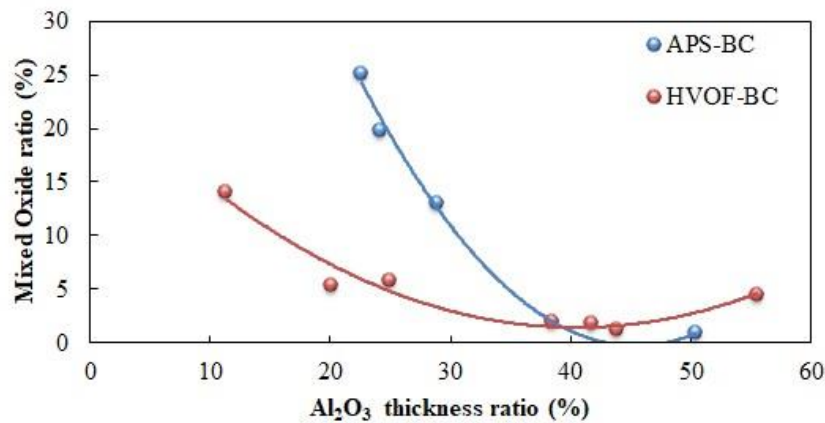


Figure 4. Mixed oxide ratio of APS-bondcoat and HVOF-bondcoat.

Table 3. Mixed oxides ratio of APS-bondcoat and HVOF-bondcoat.

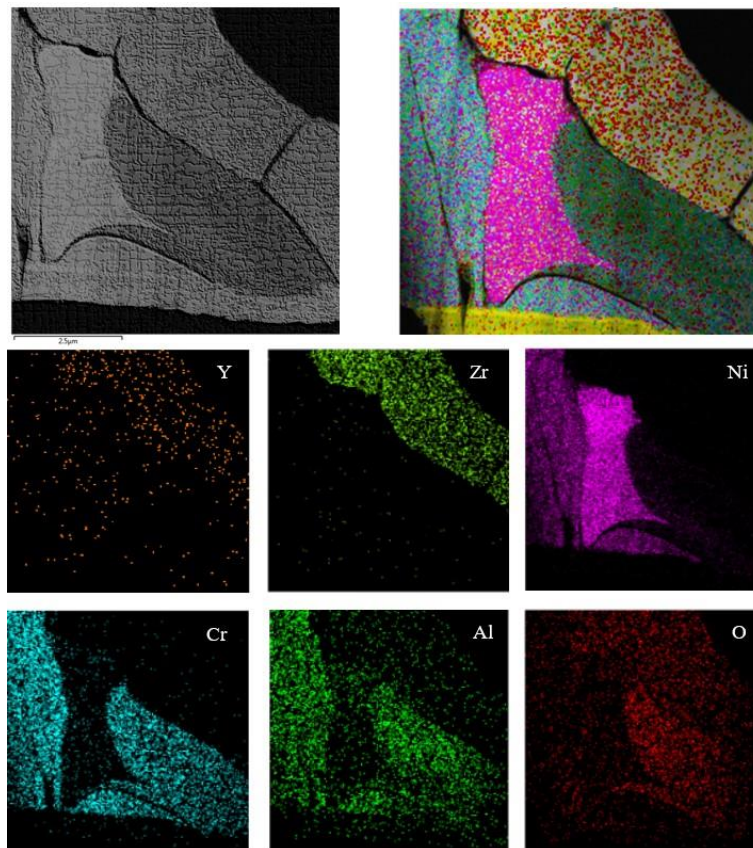
| Tests         | Samples            | Al <sub>2</sub> O <sub>3</sub> Thickness Ratio (%) |       |       |         | Mixed Oxide Ratio (%) |       |       |         |
|---------------|--------------------|--|-------|-------|---------|-----------------------|-------|-------|---------|
|               |                    | 1  | 2     | 3     | Average | 1                     | 2     | 3     | Average |
| Isothermal    | APS                | 19.40  | 21.89 | 20.90 | 20.73   | 1.32                  | 0.32  | 0.43  | 0.69    |
|               | APS-100            | 29.17  | 33.21 | 31.20 | 31.19   | 6.34                  | 7.67  | 6.93  | 6.98    |
| Thermal cycle | APS-5              | 43.22  | 44.51 | 42.56 | 43.43   | 21.34                 | 19.23 | 23.45 | 21.34   |
|               | APS-10 (failed)    | 58.38  | 61.54 | 63.45 | 61.12   | 25.34                 | 26.72 | 24.36 | 25.47   |
| Isothermal    | HVOF               | 10.65  | 12.34 | 11.54 | 11.51   | 1.18                  | 1.83  | 1.96  | 1.66    |
|               | HVOF-100           | 24.32  | 26.74 | 25.62 | 25.56   | 4.43                  | 4.56  | 4.55  | 4.51    |
| Thermal cycle | HVOF-5             | 29.45  | 30.71 | 35.81 | 31.99   | 7.82                  | 8.26  | 9.34  | 8.47    |
|               | HVOF-10            | 38.94  | 39.68 | 38.77 | 39.13   | 10.34                 | 11.28 | 11.54 | 11.05   |
|               | HVOF-1080 (failed) | 51.12  | 50.36 | 49.72 | 50.40   | 14.65                 | 14.82 | 14.10 | 14.52   |

### 3.2. Thermal Stability

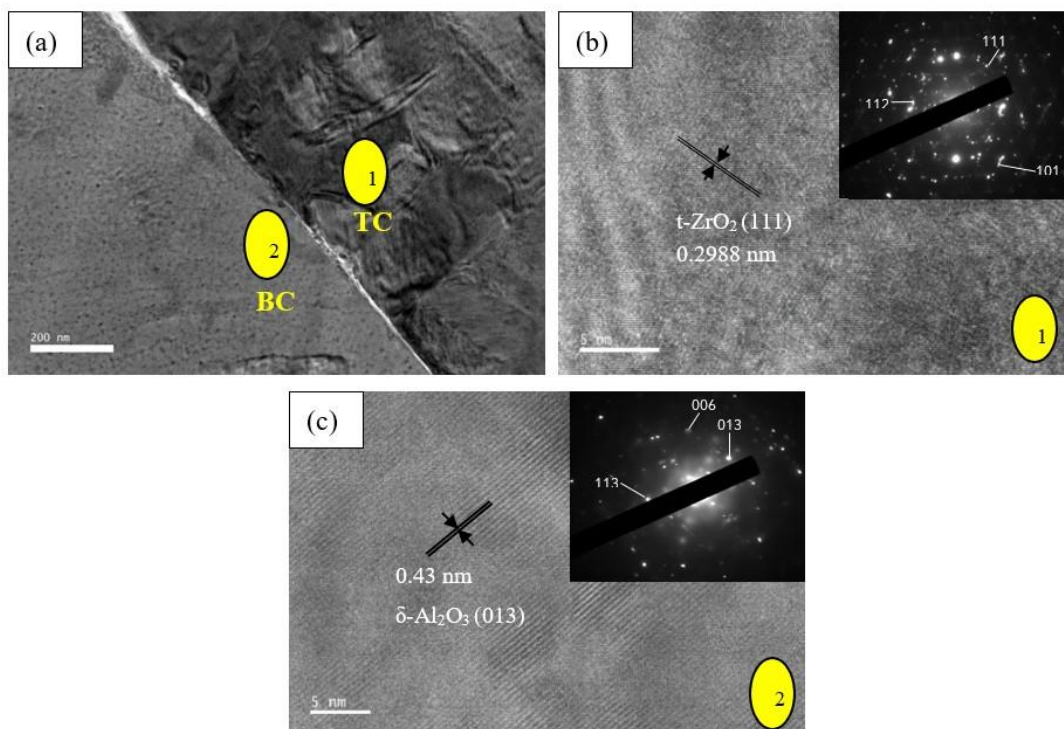
Phase changes following the temperature change determine whether the TBC system is stable in high-temperature operations. Here, phase changes were analyzed from lattice fringes via TEM. The corresponding lattice interplanar distance, *d* of the specimens is summarized in Table 4. Figures 5–16 show the EDS mapping and HRTEM images of the samples. The as-sprayed coatings are composed of tetragonal zirconia (t-ZrO<sub>2</sub>) (111). No TGO growth is observed at the interface since TGO only tends to grow at high temperatures.

Table 4. Lattice fringes of HRTEM with corresponding phases.

| Sample | Topcoat                         | TGO   | Bondcoat   |
|--------|---------------------------------|---|--|
| A      | 0.2988—t-ZrO <sub>2</sub> (111) | -   | 0.361—Cr <sub>2</sub> O <sub>3</sub> (012)<br>0.43 nm—δ Al <sub>2</sub> O <sub>3</sub> (013) |
| H      | 0.2902—t-ZrO <sub>2</sub> (112) | -   | 0.427 nm—δ Al <sub>2</sub> O <sub>3</sub> (013)  |
| A100h  | 0.2498—t-ZrO <sub>2</sub> (110) | 0.258—ZrO <sub>2</sub> (002) 0.348—α Al <sub>2</sub> O <sub>3</sub> (012)<br>0.2096—α Al <sub>2</sub> O <sub>3</sub> (113)<br>0.484—Spinel (110)<br>0.5—spinel<br>0.2095—Ni(111)          | -  |
| H100h  | 0.258—t-ZrO <sub>2</sub> (002)  | 0.438—δ Al <sub>2</sub> O <sub>3</sub> (013) 0.451—θ Al <sub>2</sub> O <sub>3</sub> (102)<br>0.245—δ Al <sub>2</sub> O <sub>3</sub> (311)<br>0.234—α Al <sub>2</sub> O <sub>3</sub> (110) | -  |
| A10c   | 0.266—c-ZrO <sub>2</sub> (111)  | 0.5—Spinel<br>0.2—α Al <sub>2</sub> O <sub>3</sub> (113)<br>0.4842—Spinel 0.2452—NiO (111)  | -  |
| H1080c | 0.3148—m-ZrO <sub>2</sub> (111) | 0.2905—c-ZrO <sub>2</sub> (111) 0.2338—α Al <sub>2</sub> O <sub>3</sub> (110)<br>0.4919—spinel (110)  | -  |



**Figure 5.** Cross-sectional microstructure and the corresponding EDS mapping of sample, A.



**Figure 6.** TEM micrograph of (a) TGO cross-sectional of sample A with interplanar distance and diffraction patterns at (b) topcoat, and (c) bondcoat.

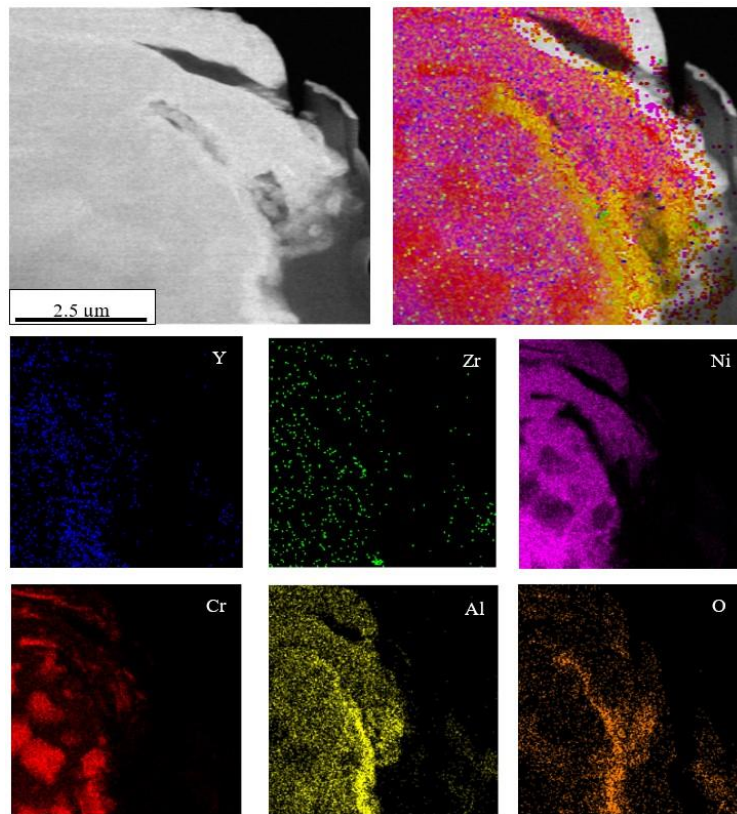


**Figure 7.** Cross-sectional microstructure and the corresponding EDS mapping of sample, H.

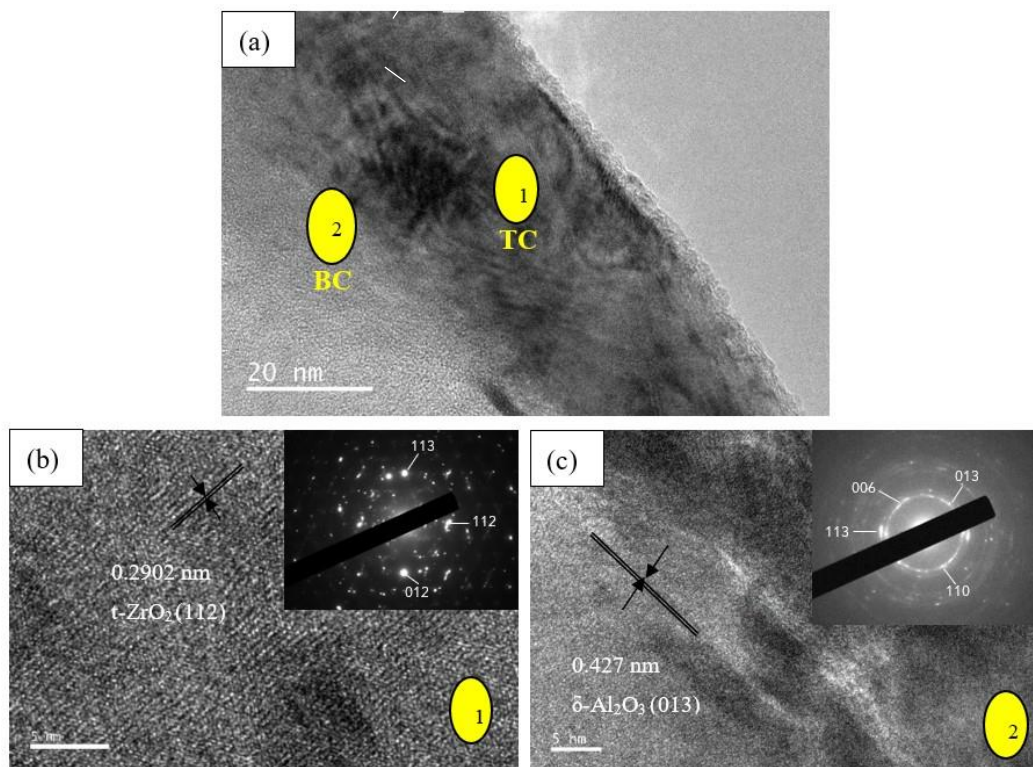


**Figure 8.** TEM micrograph of (a) TGO cross-sectional of sample H with interplanar distance and diffraction patterns at (b) topcoat, and (c) boncoat.

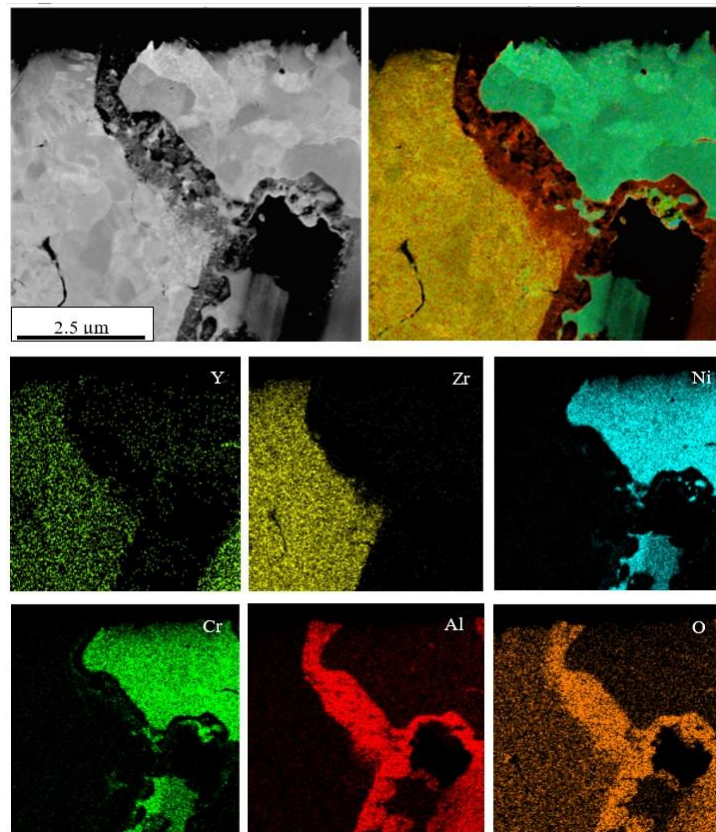


Figure 9. Cross-sectional microstructure and the corresponding EDS mapping of sample, A100h.

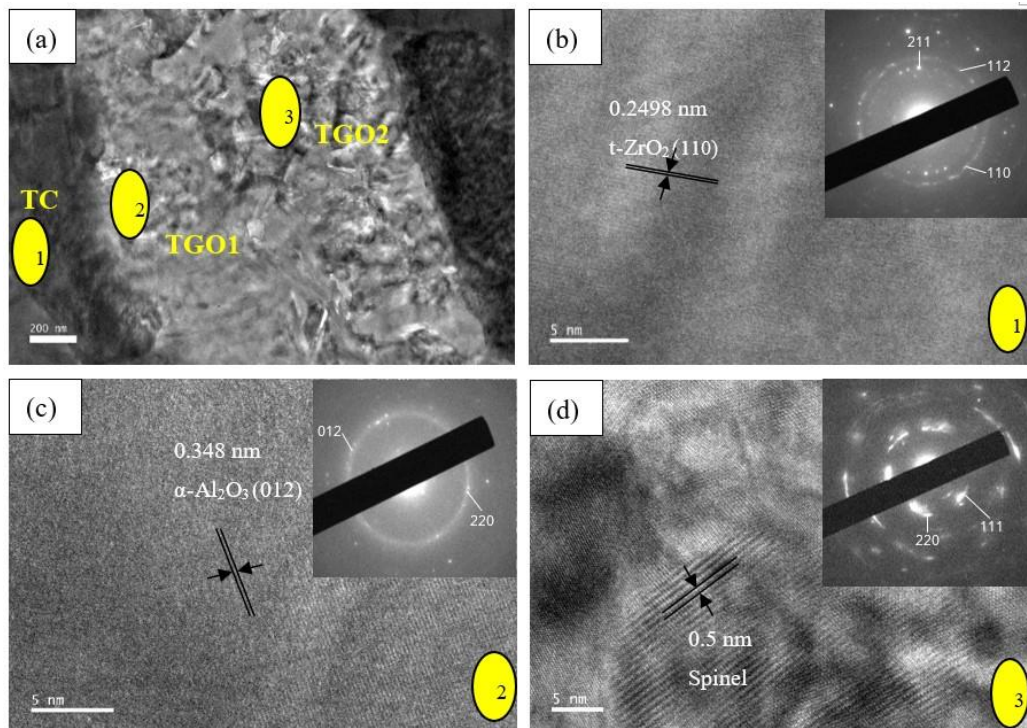
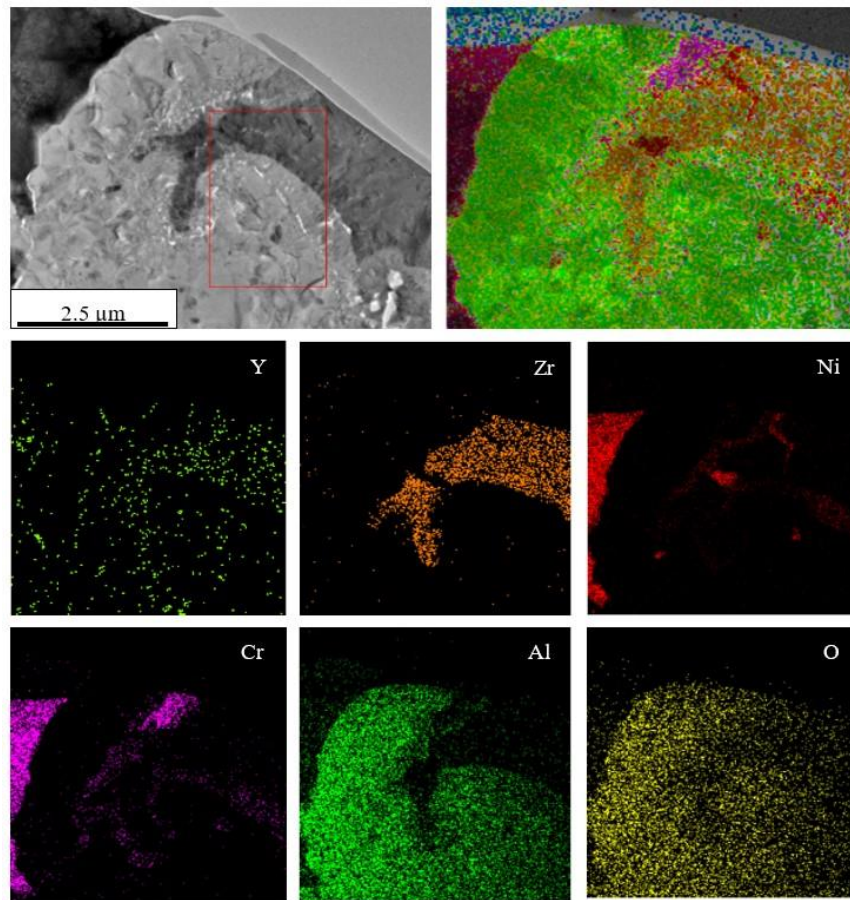
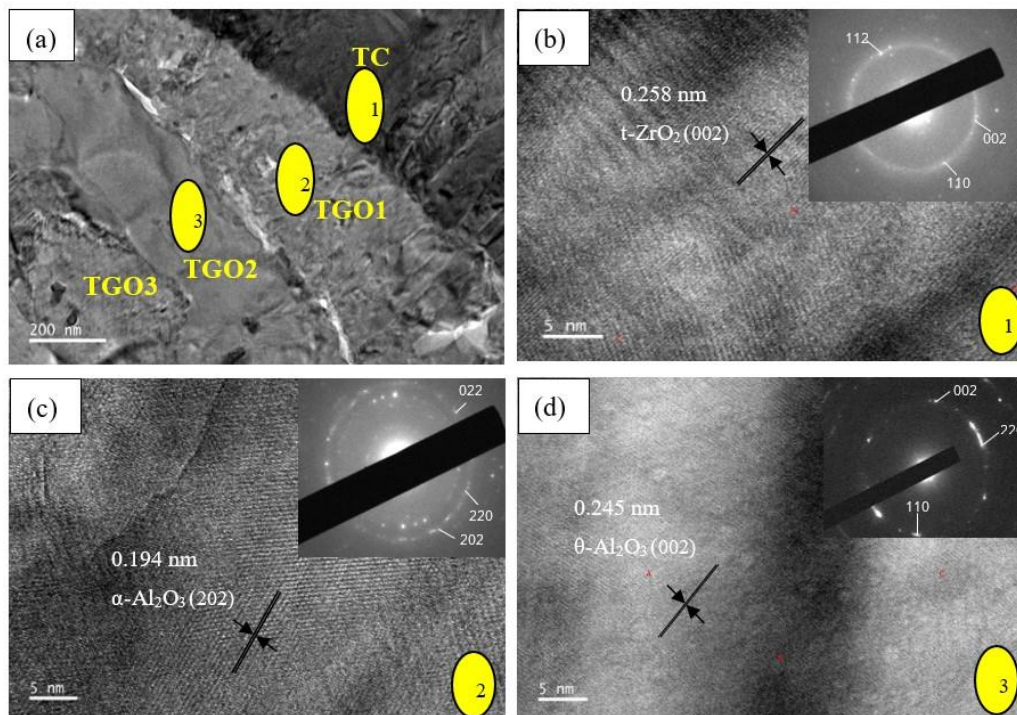


Figure 10. TEM micrograph of (a) TGO cross-sectional of sample A100h with interplanar distance and diffraction patterns at (b) topcoat, (c) TGO1, and (d) TGO2.



**Figure 11.** Cross-sectional microstructure and the corresponding EDS mapping of sample, H100h.



**Figure 12.** TEM micrograph of (a) TGO cross-sectional of sample H100h with interplanar distance and diffraction patterns at (b) topcoat, (c) TGO1, and (d) TGO2.

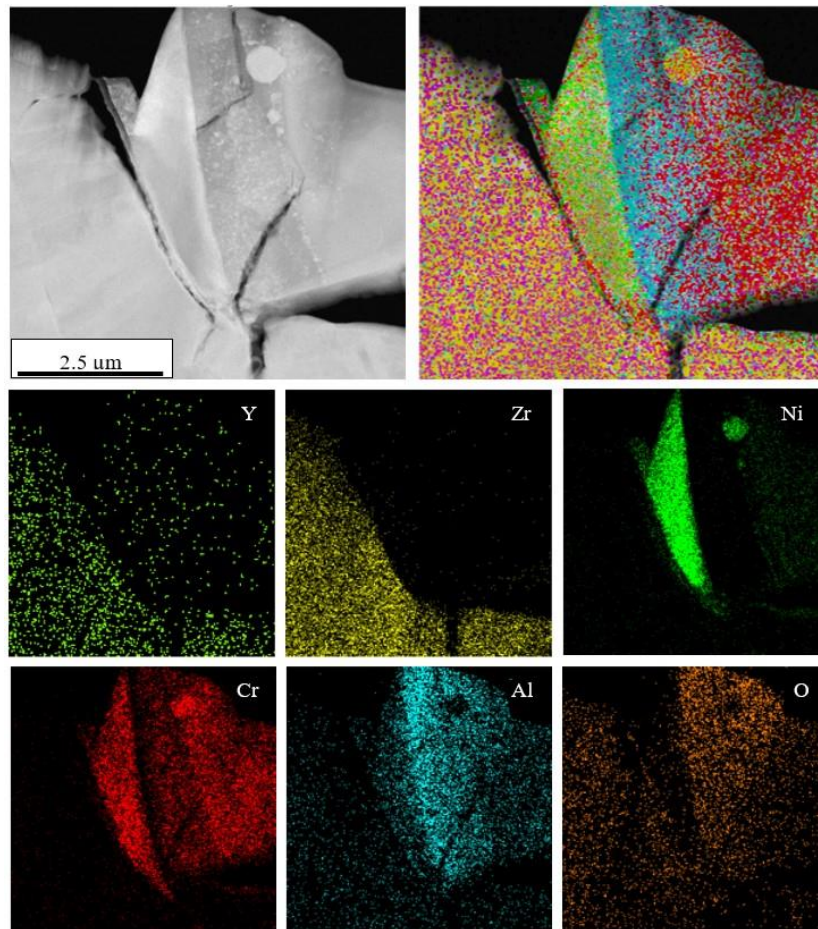


Figure 13. Cross-sectional microstructure and the corresponding EDS mapping of sample, A10c.

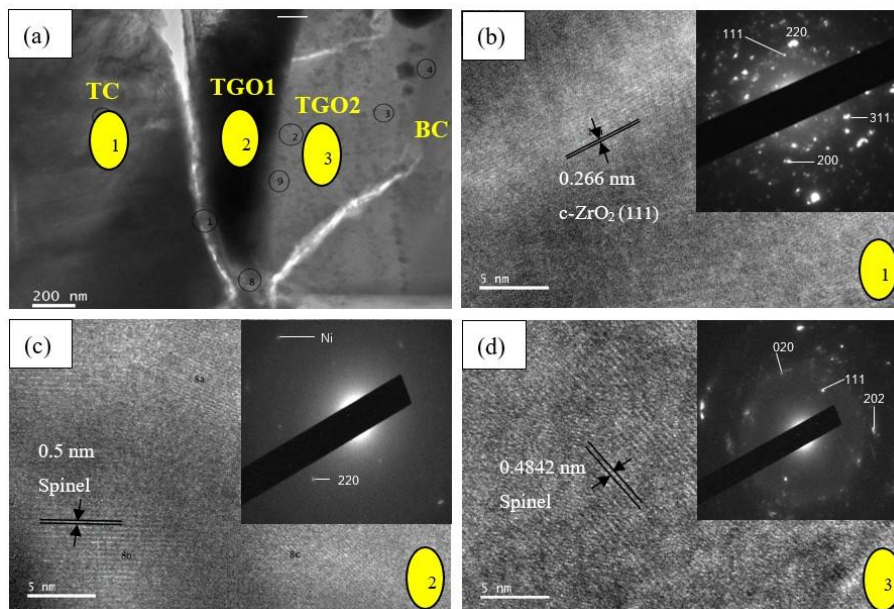
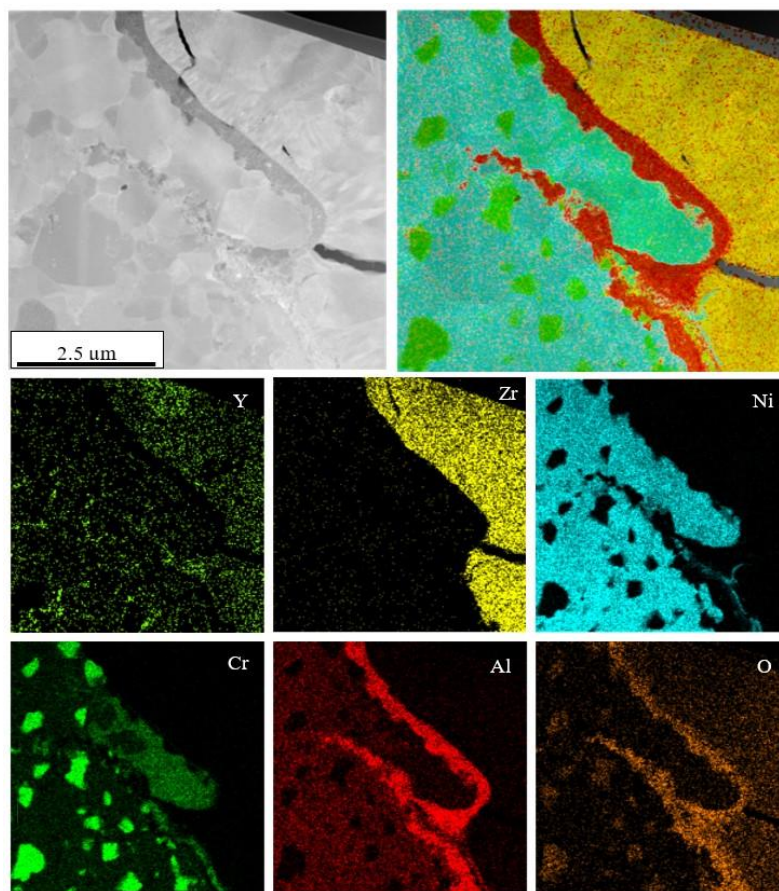
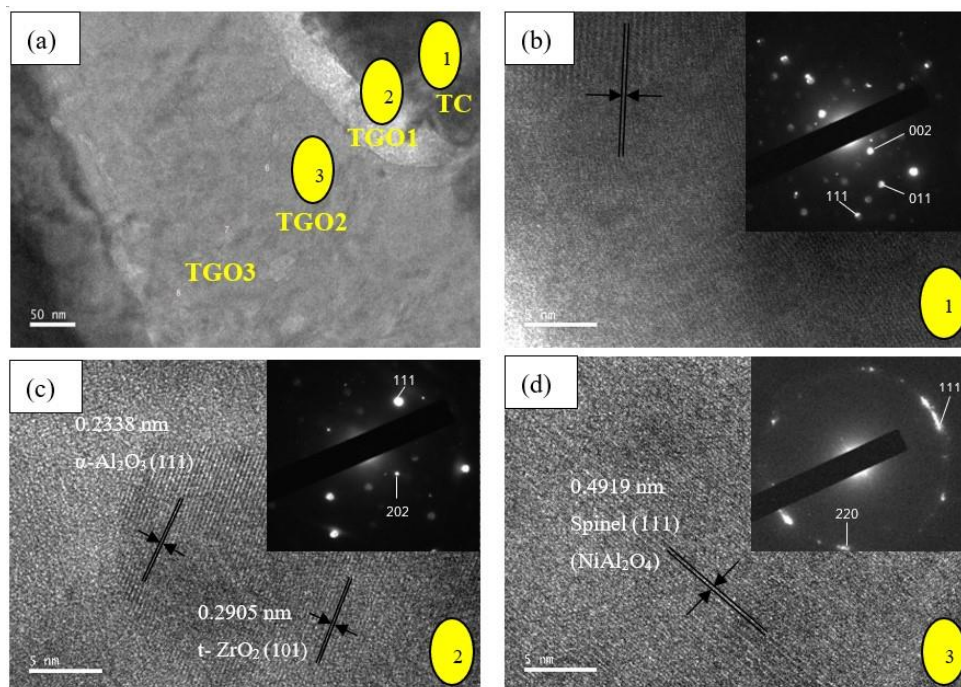


Figure 14. TEM micrograph of (a) TGO cross-sectional of sample A10c with interplanar distance and diffraction patterns at (b) topcoat, (c) TGO1, and (d) TGO2.



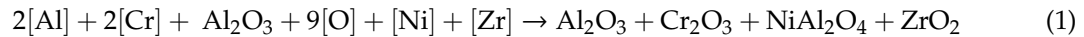
**Figure 15.** Cross-sectional microstructure and the corresponding EDS mapping of sample, H1080c.



**Figure 16.** TEM micrograph of (a) TGO cross-sectional of sample H1080c with interplanar distance and diffraction patterns at (b) topcoat, (c) TGO1, and (d) TGO2.

#### 4. Discussion

The invasive oxygen diffusion is denoted by the formation of pores (Figure 2a). The reaction among Al, Cr, Al<sub>2</sub>O<sub>3</sub>, O, Ni, and Zr is expressed in Equation (1).



The segmented layer of TGO with a higher mixed oxide ratio promoted crack propagation, with cracks appearing at the mixed oxide/TBC interface for both bondcoats (Figure 2). Although the TGO growth in HVOF consisted of an Al<sub>2</sub>O<sub>3</sub> layer and some mixed oxide clusters, the mixed oxide clusters were somewhat limited. The Al<sub>2</sub>O<sub>3</sub> layer was very stable, remaining uniform and dense up to 1079 cycles with fewer cracks. Interestingly, the vertical cracks from the top coat of HVOF did not further propagate into the TGO layer. On the other hand, cracks formed within the porous mixed oxide (NiAl<sub>2</sub>O<sub>4</sub>) layer of APS-bondcoat made it less resistant to crack propagation (Figure 2a). Sample A100h (Figure 2a) shows that it started to fail by TBC spallation, whereas the HVOF-samples remained intact with slower growth of mixed oxide from samples H1h-H1000c, in which H1080c failed at 1080 cycles.

As shown in Figures 10 and 12, there was no phase change in the coating for A100h and H100h, as both remained as t-ZrO<sub>2</sub> with (110) and (002) planes, respectively. However, it is worth highlighting that the La-Gd-YSZ could withstand the high temperature of 1400 °C until 300 h in conducting the oxidation test with an intact structure. Although phase changes were observed for the A10c (Figure 14) and H1080c (Figure 16), in which the samples failed. The tetragonal phase has been changed to cubic and monoclinic-ZrO<sub>2</sub> for A10c (111) and H1080c (111), respectively; H1080c has both a tetragonal and monoclinic structure of ZrO<sub>2</sub>. The phase changes from tetragonal to cubic or monoclinic upon cooling leads to a volume change of the coating and failure [19].

Although both topcoats of A10c (Figure 14) and H1080c (Figure 16) changed phases, APS-bondcoat failed under 10 cycles of thermal cycling, and HVOF-bondcoat failed at 1080 cycles. For A10c, the TBC spalled-off from the bondcoat and failed at an early stage, whereas H1080c failed (delamination on the surface of the topcoat) (Figure 1a) with an intact structure of the topcoat and bondcoat. This result, therefore, indicates that the type of bondcoats plays a significant role, given this different type of failure is mainly due to the TGO growth and its content that causes high stress and consequently leads to phase changes in the TBC. Besides that, δ-Al<sub>2</sub>O<sub>3</sub> (013) was seen in the bondcoat near the coating of the as-sprayed samples (Figures 6 and 8) denoting an unstable polymorph of Al<sub>2</sub>O<sub>3</sub> due to the low-temperature condition.

Additionally, significant TGO growth was observed in the samples belonging to APS-bondcoats. Here, inconsistent or segmented TGO was found in A10c (Figure 14) with high mixed oxide content such as spinel (NiAl<sub>2</sub>O<sub>4</sub>) and nickel (Ni). According to Mohd Zulkifli et al., an inconsistent TGO layer leads to the formation of a cluster of mixed oxides (due to Al depletion) that may deteriorate the durability of TBCs [32,33]. On the other hand, stable α-Al<sub>2</sub>O<sub>3</sub> was found in A100h (Figure 10), which indicates that δ-Al<sub>2</sub>O<sub>3</sub>, which was observed in the as-sprayed sample (Figures 6 and 8), had altered its phase rapidly to α-Al<sub>2</sub>O<sub>3</sub>.

Additionally, a small trace of continuous Cr layer was observed in A100h (Figure 10). Given that Cr<sub>2</sub>O<sub>3</sub> is brittle [34], an oxide can be seen growing below the α-Al<sub>2</sub>O<sub>3</sub>. Similarly, a small amount of Ni trace was also observed. Here, the presence of Al, Cr Ni, and O caused spinel to form. The low Cr content causes Ni to react with Al<sub>2</sub>O<sub>3</sub> and O<sub>2</sub> to produce spinel, as expressed in Equation (2).



Although the presence of Ni was found at the bottom of the TGO almost near the bondcoat in A100h, the detrimental NiO was not found in the TGO, given that the presence of NiO indicates complete depletion of Al and Cr, which may lead to invasive oxygen diffusion that may cause

failure [35,36]. The result reveals that A100h is in the process of failing/already failing, given the mixture of spinel and  $\alpha$ -Al<sub>2</sub>O<sub>3</sub>.

Nevertheless, sample A10c (Figure 14) shows a clear image of spallation (visible crack) between the topcoat and the TGO. However, the structure of TGO1 is very dark, given the high amount of spinel within the layer. The EDS reveals that it consists of a high amount of Ni and Cr and a low amount of Al without the presence of O. A thin layer in the top area of TGO1 is shown to exhibit more intense Cr with the area below having more intense Ni with a meager amount of Al.

The result confirms the depletion of Al in the first layer (TGO1) (Figure 14c) since Al has been consumed continuously to below the detection threshold and consists only of spinel (0.5 nm). On the other hand, TGO2 (Figure 14d) shows a high percentage of Al and O and a low percentage of Cr, and the lattice fringe confirmed  $\alpha$ -Al<sub>2</sub>O<sub>3</sub> in TGO2. As such, the results indicate that the phase had quickly changed to alpha-alumina. Moreover, NiO (0.2452 nm) was also found. When Al was depleted, NiO started to form due to the invasive Oxygen after the substantial growth of NiAl<sub>2</sub>O<sub>4</sub> (TGO1), as shown in the following equation:



Here, the thick TGO consisting of harmful mixed oxides caused high stress at the interface of topcoat/TGO and led to spallation and failure.

Contrastingly, HVOF-bondcoats (H100h and H1080c) of thinner and a continuous dense TGO layer, which acts as a protective layer to inhibit the formation of detrimental mixed oxides [37]. Sample H100h (Figure 12) shows transient aluminas of meta-stable phases ( $\eta$  and  $\theta$ ) in the TGO layer without spinel structures. The first layer of TGO (TGO1) consists of  $\delta$  and  $\theta$  aluminas with the presence of a low concentration of Cr<sub>2</sub>O<sub>3</sub>, while the second layer, also with a low level of Cr<sub>2</sub>O<sub>3</sub>, consists of  $\eta$ -Al<sub>2</sub>O<sub>3</sub> with large square-shaped grains. Typically, areas where Cr<sub>2</sub>O<sub>3</sub> develops, phase changes occur in the stages from meta-stable to  $\alpha$ -Al<sub>2</sub>O<sub>3</sub> [38]. Likewise, the formation of a low concentration of Cr<sub>2</sub>O<sub>3</sub> at an early stage of oxidation gives an epitaxial template for the TGO that promotes the kinetics of phase transformation (meta-stable phases) [38,39]. Furthermore, Cr<sub>2</sub>O<sub>3</sub> at the initial stage of oxidation on the surface of the bondcoat occurs because Cr<sub>2</sub>O<sub>3</sub> grows more quickly than Al<sub>2</sub>O<sub>3</sub> under oxidation given the lattice mismatch between Cr<sub>2</sub>O<sub>3</sub> and Ni is higher compared to the lattice mismatch between Al<sub>2</sub>O<sub>3</sub> and Ni [40,41]. The third layer (area without Cr<sub>2</sub>O<sub>3</sub>) is composed of  $\alpha$ -Al<sub>2</sub>O<sub>3</sub> with smaller grains.

Subsequently, the stage by stage phase transformation observed in H100h (Figure 12) the three significant different layers might lead to volume shrinkage from  $\delta$  to  $\alpha$  [41]. Here, the change in volume of the first and second layers causes pores to form between TGO1/TGO2 [42,43], while the decrease in volume in TGO3 (due to smaller grains) is attributed to the growth of smaller equiaxed  $\alpha$ -Al<sub>2</sub>O<sub>3</sub> grains at the expense of larger square-shaped  $\eta$ -Al<sub>2</sub>O<sub>3</sub> above it. Further to that, the grain boundaries between the delta and theta aluminas are seen. Dissimilar to the APS-bondcoat (A100h) (Figure 10), which changes quickly to  $\alpha$ -Al<sub>2</sub>O<sub>3</sub> with a mixture of spinel, H100h (Figure 12) composes of transient aluminas that change phases stages having three different significant layers from the top to bottom of the TGO.

The transient alumina phases in HVOF are due to the content of aluminum in the as-sprayed sample (Figure 8) being high. Here, more Al is present to react with Oxygen, and thus, more alumina with different phases is found in HVOF-bondcoats. The low percentage of mixed oxide in H100h (Figure 12) suggests that Ni has not changed into NiO or spinel. Here, the formation of transient aluminas has a slow growth rate of mixed oxide to form spinel. Hence, the dense TGO with stable  $\alpha$ -Al<sub>2</sub>O<sub>3</sub>, transient aluminas, and Cr<sub>2</sub>O<sub>3</sub> offer excellent protection to inhibit oxygen diffusion at the interface and make the H100h serve as a suitable TBC with an intact structure.

Likewise, H1080c (Figure 16) consists of two layers of TGO (TGO1) and (TGO2) in which the observed TGO has a consistent thickness throughout the sample. A stable, dense  $\alpha$ -Al<sub>2</sub>O<sub>3</sub> at the TGO near the topcoat (TGO1) was also observed; however, the layer below the TGO is composed of a spinel structure. Aside from that, a visible crack is seen in the topcoat approaching the TGO from the stress induced by the phase change from tetragonal to monoclinic. Although there is a long vertical crack above the TGO, the dense  $\alpha$ -Al<sub>2</sub>O<sub>3</sub> shielded the layer partially from the diffusion of Oxygen

from the topcoat and thus, protected the TBC from spallation (between the topcoat and the substrate) and remained intact. However, H1080c failed, given the high thermal cycle that caused more significant stress in the topcoat due to the phase change (t-m  $\text{ZrO}_2$ ). Since the dense  $\alpha\text{-Al}_2\text{O}_3$  shielded the layer partially, there is still inward diffusion from the topcoat leading to the formation of a spinel structure at TGO2 (below dense  $\alpha\text{-Al}_2\text{O}_3$ ). Thus, it caused the rapid creation of  $\alpha\text{-Al}_2\text{O}_3$  without the presence of transient aluminas and rapid formation to spinel.

Therefore, the result confirms that HVOF takes a longer time to form spinel by first forming transitional aluminas. While the study suggests that the thermal cycle of  $\sim 1079$  is the average threshold value for HVOF while APS bondcoat has a lower threshold to withstand a repetitive heating and cooling process to resist a cyclic load at  $1400^\circ\text{C}$ .

Indeed, these spinels lack capability in antioxidation [44]. The main reason for the formation of mixed oxide is the depletion of Al in bondcoat [45]. Besides that, NiO found in A10c (Figure 14) is also one of the main reasons for high compressive stress leading to TBC failure. Here, NiO's increased formation quickly induces a high rate of stress, which is also supported by [44], suggesting that the parabolic rate constant for NiO is typically three orders of magnitude higher than that of the protective  $\alpha\text{-Al}_2\text{O}_3$ . Hence, the expansion of the TGO layer exerts additional tension to the topcoat. As such, cracks start to propagate into interface when the intensity of the tension exceeds the cohesive strength of the PYSZ lamella.

## 5. Conclusions

In this study, oxidation and thermal-cycling tests were conducted to determine the thermal stability via HRTEM. Four types of TGO layers were found, including  $\alpha\text{-Al}_2\text{O}_3$ ,  $\alpha\text{-Al}_2\text{O}_3$  mixed with  $\text{Cr}_2\text{O}_3$ , transient aluminas, and spinel. Spinel was the most undesirable oxide since it is brittle and porous, thereby demonstrating weak adhesion to topcoat, mainly found in APS-bondcoats. The TGO of  $\alpha\text{-Al}_2\text{O}_3$  had excellent bonding to the topcoat. Simultaneously, the transient aluminas also exhibited strong adherence as it assisted in the prevention of quick  $\alpha\text{-Al}_2\text{O}_3$  transformation and the fast growth of mixed oxides. In the area where  $\text{Cr}_2\text{O}_3$  developed, the phase changed in stages from meta-stable to alpha-alumina, whereas an area without  $\text{Cr}_2\text{O}_3$  changed the phase directly to alpha-alumina. However, in APS-bondcoats, the phase quickly changed to alpha-alumina without the presence of transient aluminas, although at the same time, there were spinel and other oxides.

Therefore, this work suggests that most of the aluminum in APS-bondcoats had already started to oxidize during spraying, whereas in HVOF, since the content of Al in the as-sprayed sample was high, there was more aluminum to react with Oxygen during the operation. Thus, alumina of different phases with a dense structure and without a mixture of nickel oxide/spinel was found in HVOF. Likewise, the APS-bondcoat having a high concentration of mixed oxide led to the TBC's early spalling due to the high compressive stress present at the interface. Meanwhile, the HVOF failed only at 1080 cycles, which had a higher thermal cyclic lifetime than APS due to the repetitive heating and cooling process by the thermal cycle process, causing the phase transformation of undesired monoclinic-PYSZ, leading to high tensile stress. In order to release the strain energy, cracks were formed in the topcoat, leading to delamination. As such, the results suggest that HVOF-bondcoat has more outstanding durability than APS-bondcoat, and it is more suitable when using rare earth topcoats.

**Supplementary Materials:** The following are available online at <http://www.mdpi.com/2079-6412/10/12/1206/s1>, Figure S1: Sample characterization: (a) raw sample, (b) after cutting, and (c) rough grinding and polishing, Figure S2: Lamella thinning using focused ion beam, Figure S3: EDS spectrum and average fringe width profile frame for Sample A, Figure S4: EDS spectrum and average fringe width profile frame for Sample H, Figure S5: EDS spectrum and average fringe width profile frame for Sample A100h, Figure S6: EDS spectrum and average fringe width profile frame for Sample H100h, Figure S7: EDS spectrum and average fringe width profile frame for Sample A10c, Figure S8: EDS spectrum and average fringe width profile frame for Sample H1080c.

**Author Contributions:** All the authors have contributed to this research article such as: Conceptualization, S.M.Y. and A.M.; Data curation, S.M.Y.; Formal analysis, S.M.Y., A.M. and N.A.; Funding acquisition, S.M.Y., A.M.; Investigation, N.A., S.M. and A.M.; Methodology, S.M.Y., A.M. and N.A.; Project administration, S.M.Y.;

Resources, S.M.Y.; Software, S.M.Y., A.M. and N.A.; Supervision, A.M.; Validation, A.M.; Visualization, S.M.Y.; Writing—original draft, S.M.Y.; Writing—review and editing, A.M. All authors have read and agreed to the published version of the manuscript.

**Funding:** This research was funded by UNITEN R&D Sdn Bhd, Grant No. U-SN-CR-18-01 and UNITEN UNIIG, Grant No. J510050795. The APC was funded by UNITEN UNIIG, Grant Nos. J510050795 and MOHE grant (Grant No. 20130108FRGS).

**Acknowledgments:** The authors acknowledge Universiti Tenaga Nasional, UNITEN R&D Sdn Bhd and Institute of Sustainable Energy of UNITEN for the lab facilities. Special thanks to those who contributed directly or indirectly to this project.

**Conflicts of Interest:** The authors declare no conflict of interest. The funders had no role in the design of the study; in the collection, analyses, or interpretation of data; in the writing of the manuscript, or in the decision to publish the results.

## References

1. Kano, K.; Matsuzaki, H.; Aoyama, K.; Aoki, S.; Mandai, S. Development Study of 1500 °C Class High Temperature Gas Turbine. In Proceedings of the Turbo Expo: Power for Land, Sea, and Air, ASME 1991 International Gas Turbine and Aeroengine Congress and Exposition, Orlando, FL, USA, 3–6 June 1991; American Society of Mechanical Engineers: New York, NY, USA, 1991.
2. Ishikawa, M.; Terauchi, M.; Komori, T.; Yasuraoka, J. Development of High Efficiency Gas Turbine Combined Cycle Power Plant. *Mitsubishi Heavy Ind. Tech. Rev.* **2008**, *45*, 15–17.
3. Manap, A.; Okabe, T.; Ogawa, K.; Mahalingam, S.; Abdullah, H. Experimental and Smoothed Particle Hydrodynamics Analysis of Interfacial Bonding Between Aluminum Powder Particles and Aluminum Substrate by Cold Spray Technique. *Int. J. Adv. Manuf. Technol.* **2019**, *103*, 4519–4527. [[CrossRef](#)]
4. Xia, J.; Yang, L.; Wu, R.; Zhou, Y.; Zhang, L.; Huo, K.L.; Gan, M. Degradation Mechanisms of Air Plasma Sprayed Free-standing Yttria-stabilized Zirconia Thermal Barrier Coatings Exposed to Volcanic Ash. *Appl. Surf. Sci.* **2019**, *481*, 860–871. [[CrossRef](#)]
5. Mahalingam, S.; Mohd Yunus, S.; Manap, A.; Afandi, N.M.; Zainuddin, R.A.; Kadir, N.F. Crack Propagation and Effect of Mixed Oxides on TGO Growth in Thick La-Gd-YSZ Thermal Barrier Coating. *Coatings* **2019**, *9*, 719. [[CrossRef](#)]
6. Liu, X.; Wang, T.; Li, C.; Zheng, Z.; Li, Q. Microstructural evolution and growth kinetics of thermally grown oxides in plasma sprayed thermal barrier coatings. *Prog. Nat. Sci.* **2016**, *26*, 103–111. [[CrossRef](#)]
7. Hayase, T.; Waki, H.; Adachi, K. Residual Stress Change in Thermal Barrier Coating Due to Thermal Exposure Evaluated by Curvature Method. *J. Therm. Spray Tech.* **2020**, *29*, 1300–1312. [[CrossRef](#)]
8. Li, L.; Hitchman, N.; Knapp, J. Failure of Thermal Barrier Coatings Subjected to CMAS Attack. *J. Therm. Spray Tech.* **2010**, *19*, 148–155. [[CrossRef](#)]
9. Daroonparvar, M.; Yajid, M.A.M.; Yusof, N.M.; Hussain, M.S. Improved Thermally Grown Oxide Scale in Air Plasma Sprayed NiCrAlY/Nano-YSZ. *Coatings. J. Nanomater.* **2013**, *2013*, 1–9. [[CrossRef](#)]
10. Yajid, M.A.M.; Yusof, N.M.; Hussain, M. Formation of a dense and continuous Al<sub>2</sub>O<sub>3</sub> layer in nano thermal barrier coating systems for the suppression of spinel growth on the Al<sub>2</sub>O<sub>3</sub> oxide scale during oxidation. *J. Alloys Compd.* **2013**, *571*, 205–220. [[CrossRef](#)]
11. Wu, R.T.; Osawa, M.; Yokokawa, T.; Kawagishi, K.; Harada, H. Degradation Mechanisms of an Advanced Jet Engine Service-Retired TBC Component. *J. Solid Mech.* **2010**, *4*, 119–130. [[CrossRef](#)]
12. Patel, N.V. Use of Thermally Grown Oxide Stress Measurements to Predict Remaining Life of Thermal Barrier Coatings under Realistic Turbine Engine Conditions. Master's Thesis, University of Connecticut Graduate School, Storrs, CT, USA, 12 December 2014.
13. Stiger, M.; Yanar, N.; Jackson, R.; Laney, S.; Pettit, F.; Meier, G.; Gandhi, A.; Levi, C.G. Development of Intermixed Zones of Alumina/Zirconia in Thermal Barrier Coating Systems. *Metall. Mater. Trans. A Phys. Metall. Mater. Sci.* **2007**, *38*, 848–857. [[CrossRef](#)]
14. Kobayashi, A.; Ando, Y.; Kurokawa, K.; Hejwowski, T. Microstructure and thermal behavior of plasma sprayed zirconia/alumina composite coating. *J. Nanosci. Nanotechnol.* **2011**, *11*, 8853–8858. [[CrossRef](#)] [[PubMed](#)]

15. Huo, P.; Song, W.; Zhou, X.; Zhang, H.; Jiang, J.; Dong, S.; Cao, X.; Dingwell, D.B. Microstructures and Properties of  $\text{Sm}_2(\text{Zr}_{0.7}\text{Ce}_{0.3})_2\text{O}_7/8\text{YSZ}$  Double-ceramic-layer Thermal Barrier Coatings Deposited by Atmospheric Plasma Spraying. *J. Therm. Spray Tech.* **2019**, *28*, 986–999. [[CrossRef](#)]
16. Wang, H.; Muralidharan, G.; Leonard, D.N.; Haynes, J.A.; Porter, W.D.; England, R.D.; Hays, M.; Dwivedi, G.; Sampath, S. Microstructural Analysis and Transport Properties of Thermally Sprayed Multiple-Layer Ceramic Coatings. *J. Therm. Spray Tech.* **2018**, *27*, 371–378. [[CrossRef](#)]
17. Zhang, Q.; Xie, H.; Liu, Z.; Shi, W. Sampling Moiré Method and Its Application to Determine Modulus of Thermal Barrier Coatings under Scanning Electron Microscope. *Opt. Laser Eng.* **2018**, *107*, 315–324. [[CrossRef](#)]
18. Mutter, M.; Mauer, G.; Mücke, R.; Guillon, O.; Vaßen, R. Systematic Investigation on the Influence of Spray Parameters on the Mechanical Properties of Atmospheric Plasma-sprayed YSZ Coatings. *J. Therm. Spray Tech.* **2018**, *27*, 566–580. [[CrossRef](#)]
19. Madsen, J.; Liu, P.; Wagner, J.B.; Hansen, T.W.; Schiøtz, J. Accuracy of Surface Strain Measurements from Transmission Electron Microscopy Images of Nanoparticles. *Adv. Struct. Chem. Imag.* **2017**, *3*, 1–12. [[CrossRef](#)]
20. Béché, A.; Rouvière, J.L.; Barnes, J.P.; Cooper, D. Strain Measurement at The Nanoscale: Comparison Between Convergent Beam Electron Diffraction, Nano-beam Electron diffraction, High Resolution Imaging and Dark Field Electron Holography. *Ultramicroscopy* **2013**, *131*, 10–23. [[CrossRef](#)]
21. Hýtch, M.J.; Minor, A.M. Observing and Measuring Strain in Nanostructures and Devices with Transmission Electron Microscopy. *MRS Bull.* **2014**, *39*, 138–146. [[CrossRef](#)]
22. Vassen, R.; Cao, X.; Tietz, F.; Basu, D.; Stöver, D. Zirconates as New Materials for Thermal Barrier Coatings. *J. Am. Ceram. Soc.* **2000**, *83*, 2023–2028. [[CrossRef](#)]
23. Ma, X.; Rivellini, K.; Ruggiero, P.; Wildridge, G. Toward Durable Thermal Barrier Coating with Composite Phases and Low Thermal Conductivity. *J. Therm. Spray Tech.* **2020**, *29*, 423–432. [[CrossRef](#)]
24. Xu, Y.; Guo, X.; Lin, C.; Jiang, C.; Zheng, W.; Chang, C.; Zeng, Y. Thermal Properties and Microstructures Analysis of YSZ and YSZ- $\text{Al}_2\text{O}_3$  Thermal Barrier Coatings. *J. Therm. Spray Tech.* **2020**, *29*, 574–581. [[CrossRef](#)]
25. Mauer, G.; Du, L.; Vaßen, R. Atmospheric Plasma Spraying of Single Phase Lanthanum Zirconate Thermal Barrier Coatings with Optimized Porosity. *Coatings* **2016**, *6*, 49. [[CrossRef](#)]
26. Krämer, S.; Yang, J.; Levi, C.G. Infiltration-inhibiting Reaction of Gadolinium Zirconate Thermal Barrier Coatings with CMAS Melts. *J. Am. Ceram. Soc.* **2008**, *91*, 576–583. [[CrossRef](#)]
27. Hospach, A.; Mauer, G.; Vaßen, R.; Stöver, D. Columnar-structured Thermal Barrier Coatings (TBCs) by Thin Film Low-pressure Plasma spraying (LPPS-TF). *J. Therm. Spray Tech.* **2011**, *20*, 116–120. [[CrossRef](#)]
28. Lu, Z.; Lyu, G.; Gulhane, A.; Park, H.-M.; Kim, J.S.; Jung, Y.-G.; Zhang, J. Experimental and Modeling Studies of Bond Coat Species Effect on Microstructure Evolution in EB-PVD Thermal Barrier Coatings in Cyclic Thermal Environments. *Coatings* **2019**, *9*, 626. [[CrossRef](#)]
29. Lance, M.J.; Thiesing, B.P.; Haynes, J.A.; Parish, C.M. The Effect of HVOF Bond Coating with APS Flash Coating on TBC Performance. *Oxid. Met.* **2019**, *91*, 5–6. [[CrossRef](#)]
30. Wu, X.J.; Chen, W.R.; Patnaik, P.C. The Growth and Influence of Thermally Grown oxide in A Thermal Barrier Coating. In *Proceedings of the Thermal Spray 2007: Global Coating Solutions, Beijing, China, 14–16 May 2007*; Marple, B.R., Hyland, M.M., Lau, Y.-C., Li, C.-J., Lima, R.S., Montavon, G., Eds.; ASM Thermal Spray Society, ASM International: Novelty, OH, USA, 2007; pp. 446–451.
31. Brinkman, H.W.; Briels, W.J.; Verweij, H. Molecular Dynamics Simulations of Yttrium-stabilized Zirconia. *Chem. Phys. Lett.* **1995**, *247*, 386–390. [[CrossRef](#)]
32. Bengtsson, P.; Ericsson, T.; Wigren, J. Thermal Shock Testing of Burner Cans Coated with a Thick Thermal Barrier Coating. *J. Therm. Spray Technol.* **1998**, *7*, 340–348. [[CrossRef](#)]
33. Mohd Zulkifli, S.; Mat Yajid, M.A.; Idris, M.H.; Daroonparvar, M.; Hamdan, H. TGO Formation with NiCoCrAlYTa Bond Coat Deposition using APS and HVOF Method. *Adv. Mat. Res.* **2015**, *1125*, 18–22. [[CrossRef](#)]
34. Vernhes, L.; Bekins, C.; Lourdel, N.; Poirier, D.; Lima, R.; Li, D.; Klemberg-Sapieha, J. Nanostructured and Conventional  $\text{Cr}_2\text{O}_3$ ,  $\text{TiO}_2$ , and  $\text{TiO}_2\text{-Cr}_2\text{O}_3$  Thermal-Sprayed Coatings for Metal-Seated Ball Valve Applications in Hydrometallurgy. *J. Therm. Spray Technol.* **2016**, *25*, 1068–1078. [[CrossRef](#)]
35. Liu, Y.Z.; Zheng, S.J.; Zhu, Y.L.; Wei, H.; Ma, X.L. Microstructural Evolution at Interfaces of Thermal Barrier Coatings During Isothermal Oxidation. *J. Eur. Ceram. Soc.* **2016**, *36*, 1765–1774. [[CrossRef](#)]

36. Daroonparvar, M.; Yajid, M.A.; Yusof, N.M.; Farahany, S.; Hussain, M.S.; Bakhsheshi-Rad, H.R.; Valefi, Z.; Abdolahi, A. Improvement of Thermally Grown Oxide Layer in Thermal Barrier Coating Systems with Nano Alumina as Third Layer. *T. Nanferr. Metal Soc.* **2013**, *23*, 1322–1333. [[CrossRef](#)]
37. Daroonparvar, M.; Hussain, M.S.; Mat Yajid, M.A. The Role of Formation of Continues Thermally Grown Oxide Layer on the Nanostructured NiCrAlY Bond Coat During Thermal Exposure in Air. *Appl. Surf. Sci.* **2012**, *261*, 287–297. [[CrossRef](#)]
38. Fujita, M.; Inukai, K.; Sakida, S.; Nanba, T.; Ommyoji, J.A. Yamaguchi, and Y. Miura, Sintering of Al<sub>2</sub>O<sub>3</sub>-Cr<sub>2</sub>O<sub>3</sub> Powder Prepared by Sol-gel Process. *J. Soc. Mater. Sci. Jpn.* **2007**, *56*, 526–530. [[CrossRef](#)]
39. Peng, X.; Clarke, D.R.; Wang, F. Transient-alumina Transformations during the Oxidation of Magnetron-sputtered CoCrAl Nanocrystalline Coatings. *Oxid. Met.* **2003**, *60*, 225–240. [[CrossRef](#)]
40. Liang, G.Y.; Zhu, C.; Wu, X.Y.; Wu, Y. The Formation Model of Ni-Cr Oxides on NiCoCrAlY-Sprayed Coating. *Appl. Surf. Sci.* **2011**, *257*, 6468–6473. [[CrossRef](#)]
41. Kolarik, V.; Juez-Lorenzo, M.; Fietzek, H. Oxidation of Micro-Sized Spherical Aluminum Particles. *Mater. Sci. Forum* **2011**, *696*, 290–295. [[CrossRef](#)]
42. Manap, A.; Nakano, A.; Ogawa, K. The Protectiveness of Thermally Grown Oxides on Cold Sprayed CoNiCrAlY Bond Coat in Thermal Barrier Coating. *J. Therm. Spray Technol.* **2012**, *21*, 586–596. [[CrossRef](#)]
43. Nijdam, T.J.; Sloof, W.G. Microstructural Evolution of a MCrAlY Coating upon Isothermal Annealing. *Mater. Charact.* **2008**, *59*, 1697–1704. [[CrossRef](#)]
44. Teixeira, V.; Andritschky, M.; Fischer, W.; Buchkremer, H.P.; Stöver, D. Effects of Deposition Temperature and Thermal Cycling on Residual Stress State in Zirconia-based Thermal Barrier Coatings. *Surf. Coat. Technol.* **1999**, *120–121*, 103–111. [[CrossRef](#)]
45. Matsumoto, M.; Hayakawa, K.; Kitaoka, S.; Matsubara, H.; Takayama, H.; Kagiya, Y.; Sugita, Y. The Effect of Preoxidation Atmosphere on Oxidation Behavior and Thermal Cycle Life of Thermal Barrier Coatings. *Mater. Sci. Eng. A Struct.* **2006**, *441*, 119–125. [[CrossRef](#)]

**Publisher's Note:** MDPI stays neutral with regard to jurisdictional claims in published maps and institutional affiliations.



© 2020 by the authors. Licensee MDPI, Basel, Switzerland. This article is an open access article distributed under the terms and conditions of the Creative Commons Attribution (CC BY) license (<http://creativecommons.org/licenses/by/4.0/>).